Journal of Materials Chemistry A

Accepted Manuscript

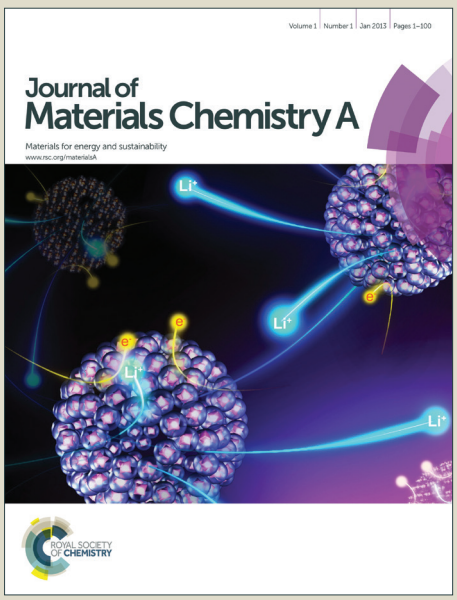

ROYAL SOCIETY OF CHEMISTRY

www.rsc.org/materialsA

Journal Name

RSCPublishing

ARTICLE

High-Power and High-Energy Asymmetric Supercapacitors Based on Li^+-intercalation into *T*-Nb_2O_5/Graphene Pseudocapative Electrode

Lingping Kong,[a] Chuanfang Zhang, [a] Songmin Zhang, [a] Jitong Wang, [a] Rong Cai,[b] Chunxiang Lv,*[b] Wenming Qiao, [a] Licheng Ling [a] and Donghui Long* [a]

Cite this: DOI: 10.1039/x0xx00000x

Received 00th January 2012,
Accepted 00th January 2012

DOI: 10.1039/x0xx00000x

www.rsc.org/

The intercalation pseudocapacitance which leads to the extraordinary charge storage properties has been confirmed as an intrinsic capactive property of orthorhombic Nb_2O_5 (*T*-Nb_2O_5) nanocrystals. However, the poor electronic conductivity of *T*-Nb_2O_5 nanocrystals may limit its electrochemical utilization and high-rate performance especially for thick electrodes with high mass loadings. To address this issue, we herein reported a hydrothermal-heat treatment method to anchor *T*-Nb_2O_5 nanocrystals on conductive graphene sheets, which forms a layer-by-layer integrated electrode with much shortened ion transport paths and results in excellent electrochemical capacitive properties, including high capacitance (626 C g^{-1}), excellent rate handling and cyclic stability. Furthermore, asymmetric supercapacitors were constructed by using the high-rate response *T*-Nb_2O_5/graphene nanocomposite and mesoporous carbon as the negative and positive electrode, respectively. The asymmetric supercapacitor could deliver a high energy density of 16 Wh kg^{-1} at an unprecedented power density of 45 kW kg^{-1} (discharge time of 1.2 s). The outstanding power properties of the supercapacitors are mainly attributed to the improved high-rate Li-insertion/extraction capability of the *T*-Nb_2O_5/graphene electrode and appropriate pairing of mesoporous carbon electrode.

1. Introduction

Charge storage mechanisms for supercapacitors generally include the charge separation at the electrode-electrolyte interface (electric double layer capacitor, EDLC) and fast surface faradaic reactions (pseduocapacitor).[1-4] Recently, it was found that fast Li-ion (Li^+) intercalation/extraction could occur not only at the surface but also in the bulk of the orthorhombic Nb_2O_5 (*T*-Nb_2O_5) nanocrystals in non-aqueous Li^+ electrolyte.[5-10] The unique *T*-Nb_2O_5 nanocrystals could offer two-dimensional Li^+ transport pathways with almost no kinetics limitations from solid-state diffusion, giving rise to a intrinsic pseudocapacitive behavior observed in the bulk intercalaction material. Because the whole bulk of *T*-Nb_2O_5 nanocrystals could be utilized for capative energy storage, the theoretical capacitance for *T*-Nb_2O_5 is as high as 720 C g^{-1} according to the electron transfer reaction (Nb^{5+}/Nb^{3+}).[11-14] In addition, the use of non-aqueous Li^+ electrolyte provides a wide potential window, leading to higher energy density than in conventional carbon-based supercapacitors.

Similar to most pseudocapacitive metal oxide materials, however, *T*-Nb_2O_5 is also an electronic semi-conductor with a bulk electrical conductivity of ~3.4×10^{-6} S cm^{-1} at 300K and a bandgap of ~3.4 eV.[15-17] Thus, when *T*-Nb_2O_5 nanocrystals were fabricated into a relatively thick electrode, the power handling property would be limited due to the sluggish mobility of electrons.[9] A possible effective method to improve the power handling is by depositing the pseudocapacitive metal oxides such as RuO_2,[18,19] MnO_2,[20,21] Co_3O_4,[22] V_2O_5,[23] NiO_x[24] uniformly onto the conductive materials, which could expose more redox active nanoparticles to the electrolyte as well as greatly improve the electronic conductivity.[25] Unfortunately, only a few works have been reported to prepare conducting Nb_2O_5 composites with fast electron transportation and ion diffusion kinetics. Recently, Wang et al made a first try to physically mixed the Nb_2O_5 nanoparticles and carbon nanotubes (CNTs) during the electrode slurry preparation.[26] The introduction of CNTs networks could enable fast electron transport and effectively improve rate capability. However, the physical mixing of CNT and Nb_2O_5 nanoparticles is more like increasing the amount of conductive agent, which fails to

fullfill a good interfacial interactions between CNT and nanoparticles, especially after repeated charge-discharge cycles. Hence developing a general and effective chemical approach to construct conductive *T*-Nb_2O_5 composites, especially with well-defined orthorhombic Nb_2O_5 structure, high active material mass loading, sufficient electronic conductivity and direct exposure of the active sites to the electrolyte, still remains a great challenge.

Graphene has been considered a promising candidate as a supercapacitor electrode material due to its attractive characteristics such as large surface area, good flexibility, excellent electrical conductivity and wide potential windows. [27-33] The intrinsic capacitance of single-layer graphene reaches ca. 21 μFcm $^{-2}$ when the entire surface area is used.[30] It is also an excellent substrate to host active nanomaterials for charge storage due to its abundant surface functional groups.[34-36] Recent advances on graphene/metal oxide composites for the electrochemial applications[34-38] inspired us to syntheize the *T*-Nb_2O_5/graphene nanocomposites, which may greatly improve the utilization of active *T*-Nb_2O_5 nanocrystals and consequently achieve excellent performance.

Herein, we present a simple and one-pot hydrothermal method to decroate Nb_2O_5 nanoparticles onto the surface of reduced graphene oxides (rGO) sheets. After post-heatment at 700 ^{o}C, rGO converted into graphene with improved electric conductivity while the amorphous Nb_2O_5 nanoparticles recrystallized into *T*-Nb_2O_5 nanocrystals. The synergistic effects between graphene and *T*-Nb_2O_5 nanocrystals result in excellent electrochemical capaitive properties including high capacitance, increased rate capability and excellent cyclic stability. Furthermore, a asymmetric cell comprised of a *T*-Nb_2O_5/graphene negative electrode and porous carbon positive electrode was assembled. Unlike the conventional asymmetric supercapacitors which comprise battery-like Li-ion intercalating electrode and EDLC-forming counter electrode,[39-42] the asymmetric cells present here were constructured by both high-rate response electrodes, which resulted in very excellent capacitive performance at the high current loading, energy density, power delivery and cycle life. To our knowledge, this is the first time that *T*-Nb_2O_5/graphene nanocomposites are prepared and further paired up with mesoporous carbons to produce high-power-density supercapacitors with reasonable energy density. This asymmetric supercapacitor approach is able to fill the gap between batteries and conventional capacitors without sacrificing power delivery and cycle life, being attractive for a wide range of surge-power delivery applications.

2. Experimental section

2.1. Synthesis of graphite oxide (GO)

GO was synthesized according to the modified Hummers method[40] where natural graphite flakes were oxidized using $KMnO_4$, $NaNO_3$, and 98% H_2SO_4 as the strong oxidant. The graphite oxide dispersion in DI-waterwas sonicated for 1.5 h. The resultant homogeneous brown GO dispersion (5 mg/mL) was stable for months and directly used without further treatment.

2.2. Preparation of Nb_2O_5/rGO nanocomposites and *T*-Nb_2O_5/graphene nanocomposites

A one-pot hydrothermal method has been developed to synthesize the Nb_2O_5/rGO nanocomposites. Typically, 0.2 g Pluronic P123 (Sigma) was dissolved in 20 mL DI-water, then 20 mL GO solution (5 mg/mL) was added into the solution under stirring. The obtained P123/GO solution was sonicated for 10 min. On the other hand, 1.14 g ammonium niobate oxalate hydrate ($C_4H_4NNbO_9 \cdot xH_2O$, Sigma) was dissolved in 20 mL DI-water. Then, the ammonium niobate solution and HCl (2 M, 5 drops) was added into the P123/GO solution under the magnetic stirring, giving rise to a homogenous solution. The solution was transferred to an 80 mL Teflon-lined autoclave and heated at 180 ^{o}C for 24 h. The resulting products were collected, filtered, washed with DI water and ethanol alternatively several times, and then dried to obtain Nb_2O_5/rGO nanocomposite. Finnally, the dried solids were heat-treated at 700 ^{o}C for 3 h with a heating rate of 2 °C min^{-1} in N_2 flow, yielding the *T*-Nb_2O_5/graphene nanocomposites. For comprasion, pure *T*-Nb_2O_5 nanoparticles were also prepared using the same procedure but without the adding of GO solution.

Commerically available activated carbons for EDLC (KOH-H_2 treated carbons) were purchased from Shanghai Carbosino Material Co.Ltd. The mesoporous carbons were prepared by a colloid silica template using the resorcinol-formardlehyde as carbon precusors and hydrolysized silica sol as hard template, according to our previous report.[44]

2.3. Material characterizations

The morphology and microstructure of the samples were observed on field emission scanning electron microscopy (SEM, FEI-300) and transmission electron microscopy (TEM, JEOL, 2100F). The crystalline structure of each samples was identified by a powder X-ray diffraction (XRD) patterns with a RigakuD/max 2550 diffractometer operating at 40 kV and 20 mA using Cu Ka radiation (0.15406 nm). The Raman spectra of each sample was recorded at room temperature on a Spex 1403 Raman spectrometer with an argon ion laser at an excitation wavelength of 514.5 nm. Thermogravimetric analysis (TGA) patterns were performed using TA Instrument Q600 Analyser from room temperature to 800 ^{o}C at a rate of 10 ^{o}C min^{-1} in the air flow. Specific surface area was measured by the Nitrogen adsorption-desorption isotherms.

2.4. Electrode fabrication

The slurry of *T*-Nb_2O_5/graphene nanocomposite was prepared by mixing the active material, carbon black (Timical super C65) and polyvinylidene fluoride (PVDF) binder in a 8:1:1 weight ratio in N-methyl-2-pyrrolidinone (NMP). Then the slurry was casted onto copper foil, dried in a 80 ^{o}C in a vacuum

oven, and punched into electrodes with a diameter of 12 mm and a thickness of 30 μm (excluding thickness of Cu foil) .

To prepare porous carbon electrodes, microporous activated carbons or mesoporous carbons were mixed with carbon black and polytetrafluoroethylene binder (PTFE, 60 wt% in H_2O) in a mass ratio of 85:10:5. The slurry was well grounded in ethanol until a homogeneous paste was formed. The paste was cold-rolled into a film and then punched into electrode with diameter of 12 mm and controllable thickness of 100-150 μm. All the electrodes were dried at 110 °C in a vacuum oven for 12 h.

2.5. Electrochemical tests

The electrochemical properties of *T*-Nb_2O_5/graphene nanocomposite were characterized using 3-electrode setup in 1 M $LiPF_6$ in EC/DMC/EMC (V/V, 1:1:1). Cyclic voltammetry (CV) at different scan rates (range from 2 to 200 mV s^{-1}) and Electrochemical impedance spectroscopy (EIS) were conducted on PCI-4/300 potentiostat (Gamry, USA), galvanostatic charge-discharge (GCD) tests were conducted on the Arbin BT2000 system. The *T*-Nb_2O_5/graphene nanocomposite worked as working electrode, overcapacitive activated carbons and lithium foil were used as counter and reference electrode, respectively. The potential of working electrode was set to 1.0 - 3.0 V (vs. Li^+/Li). the separator was a microporous membrane (Celgard 2400). All the cells were assembled in an argon filled glove box at 25 °C. The weight of total *T*-Nb_2O_5/graphene nanocomposites was used to calculate the gravimetrically normalized current and capacitance.

The hybrid cells were assembled using *T*-Nb_2O_5/graphene as negative electrode, microporous or mesoporous carbons as positive electrode, respectively. The loading mass ratio between each carbon materials and *T*-Nb_2O_5/graphene nanocomposites was optimized according the specific capacitance calculated from their discharge curves, respectively. The optimal mass ratio between the positive and negative electrodes is obtained when the charge (q) strikes balance across the two electrodes ($q_+=q_-$). The charge stored by each electrode usually depends on the specific capacitance (C), the work operating voltage (ΔE) and the mass of the electrode (m) following Equation

$$q=C\times\Delta E\times m \quad (1)$$

then the mass ratio of two electrodes should follow:

$$m_+/m_-=(C_-\times\Delta E_-)/(C_+\times\Delta E_+) \quad (2)$$

In this work, the mass ratio of positive/negative active material was set to 3.5 for activated carbons couped cells and 3.7 for mesoporous carbons couped cells.

The energy density (E) of the cells can be achieved by the specific capacitance (C, based on the mass of total active materials) and the cell voltage (V) according to the following equation:

$$E=0.5\,CV^2\ (\text{Wh kg}^{-1}) \quad (3)$$

The power density (P) of the cells can be achieved by the energy density (E) and the discharging time (t) according to the following equation:

$$P=E/t\ \ (\text{kW kg}^{-1}) \quad (4)$$

3. Results and discussion

Fig. 1a shows the schematic of the *T*-Nb_2O_5/graphene nanocomposites' preparation. The anchoring of tiny Nb_2O_5 nanoparticles onto GO surface was achieved by the hydrothermal of niobium precursor. Amorphous Nb_2O_5 nanoparticles decorated composite was achieved, as revealed by XRD patterns in Fig. 1b and Raman spectra in Fig. 1c. In addition, it can also concluded that the GO could be partially reduceded into rGO after hydrothermal treatment at 180 °C , as the GO characterstic peak (2θ ~10°) disappears in the XRD pattern. After further heat-treatment at 700 °C, the amorphous Nb_2O_5 is converted into highly crystallized Nb_2O_5 with a orthorhombic structure (JCPDS 30-0873).[5,14] The specific Raman vibrational modes centred at 260.0 cm^{-1} (v_6), 660 cm^{-1} (v_2) and 980 cm^{-1} (v_1) aslo confirm that the Nb_2O_5 nanocrsytals are orthorhombic phase.[45,46] The peak intensity ratio of D and G bands (I_D/I_G) in Raman sepctra provides information about the structural evolution of GO during hydrothermal and heat-treatment process. In the present case, the I_D/I_G ratios are 0.63 for GO, and 0.98 for rGO and 1.02 for graphene. This result indicates new graphitic domains are created that are smaller in size to the ones present in GO during hydrothermal and heat-treatment process.[47]

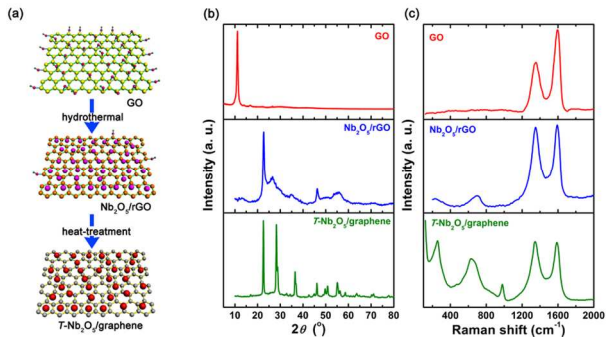

Fig. 1 (a) Schematic diagram of the fabrication of the *T*-Nb_2O_5/graphene nanocomposites; (b) XRD patterns and (c) Raman spectra of GO, Nb_2O_5/rGO and *T*-Nb_2O_5/graphene.

Journal Name

RSCPublishing

ARTICLE

The weight percent of graphene in the nanocomposites was determined to be 10 wt% by TG analysis in air flow (Fig. S1). It should be noted that the weight ratio of graphene can be easily adjusted by changing the amount of GO solution. For example, the *T*-Nb_2O_5/graphene nanocomposites with 25 wt% graphene were also prepared with similar physichemical properties (Fig. S2). The pure Nb_2O_5 sample prepared using similar conditions except without GO addition has also proved as *T*-Nb_2O_5 nanocrsytals in the XRD profiles (Fig. S3).

Fig. 2 shows SEM and TEM images of the samples. The hydrothermal product Nb_2O_5/rGO shows some small rod-like nanopartiles aggregated on the surface of rGO (Fig. 2a and d). After thermal treatment, the *T*-Nb_2O_5/graphene nanocomposites show a curled morphology, consisting of a thin wrinkled "paperlike" structure with some aggregated *T*-Nb_2O_5 nanocrystals (Fig. 2b). The typical Nb_2O_5 particle size is 20-40 nm, which can be further confirmed by the TEM image in Fig. 2e. The high-resolution TEM image in Fig. 2f shows the interface between graphene and *T*-Nb_2O_5 nanocrystals. The lattice fringes having an interlayer distance of 0.393 nm agrees well with the spacing between (001) planes of *T*-Nb_2O_5 crystals. It should be emphasized that, even after a long time of sonication during the preparation of the TEM specimen, the *T*-Nb_2O_5 nanocrystals are still strongly anchored on the surface of graphene sheets with a high density, as shown in Fig. 2e, suggesting the strong interaction between nanocrystals and graphene sheets. Meanwhile, the presence of *T*-Nb_2O_5 nanocrystals can efficiently suppresss the re-stacking of graphene layers, building a 3D interconnected conductive porous network for charge transportation. In contrast, severe aggregated particles are observed in case of pure *T*-Nb_2O_5 in Fig. 2c.

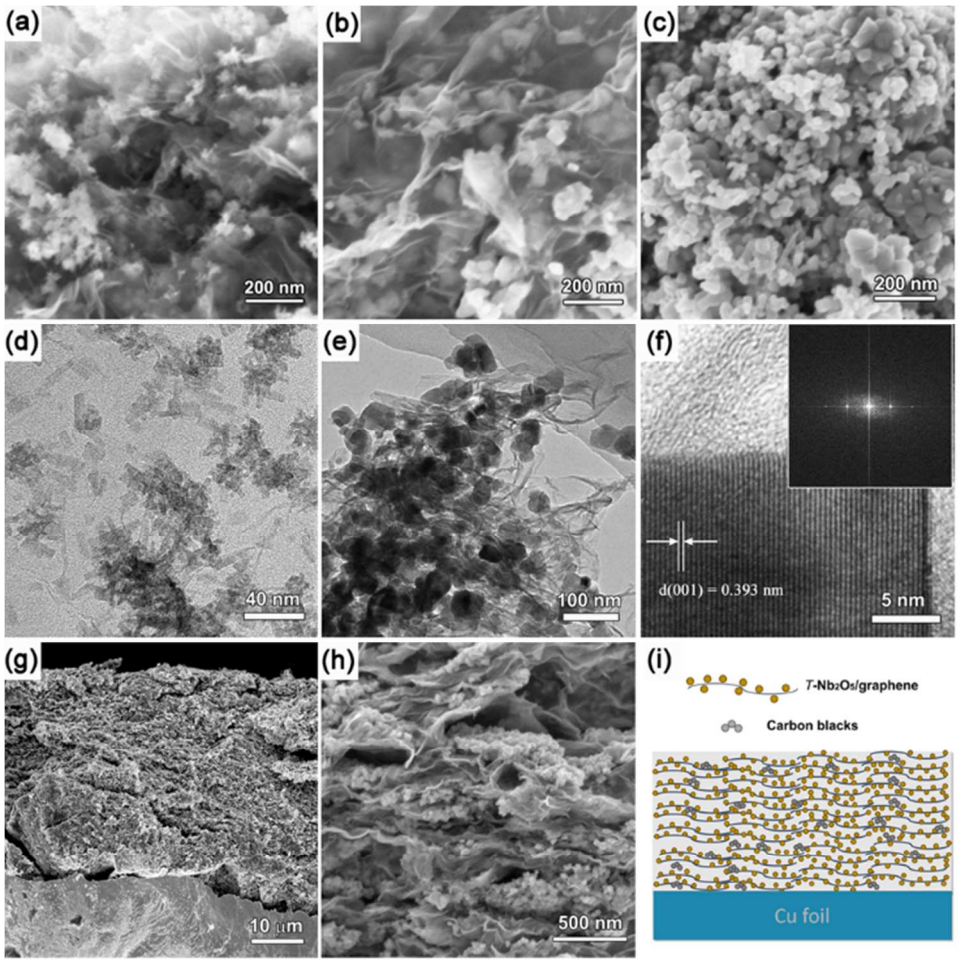

Fig.2 SEM images: (a) Nb_2O_5/rGO, (b) *T*-Nb_2O_5/graphene and (c) *T*-Nb_2O_5, TEM images: (d) Nb_2O_5/rGO and (e) *T*-Nb_2O_5/graphene, (f) HR-TEM image of *T*-Nb_2O_5/graphene, (g), (h) SEM images of cross-section of *T*-Nb_2O_5/graphene electrode film, (i) schematic diagram of the *T*-Nb_2O_5/graphene electrode.

Journal Name

RSCPublishing

ARTICLE

The porous characteristics of the samples were investigated by a nitrogen adsorption-desorp tion measurement (Fig. S4). The BET specific surface area of *T*-Nb_2O_5/graphene nanocomposite is 104 m^2 g^{-1}, higher than that of pure *T*-Nb_2O_5 (39 m^2 g^{-1}). In addition, the *T*-Nb_2O_5/graphene nanocomposite possesses a certain amount of macropores and mesopores with pore volume of 0.33 cm^3 g^{-1} that issues form a sheet-like porous system. Such open porous system should facilitate electrolyte ion diffusion to active sites more efficiently.

The cross-section SEM image of the eletrode show a well-organized layer-by-layer assembled structure consisting of graphene sheet and *T*-Nb_2O_5 particles with a film thickness of ~ 30 μm (Fig. 2g). The compact film has a high mass loading of ca. 1.2 mg cm^{-2} and the pack density of 400 mg cm^{-3}. The flexible layered structure of *T*-Nb_2O_5/graphene nanocomposite is beneficial in constructing an effective electron transportation highway, and is expected to keep the structural stability and electrode integrity during the repeated charge-discharge process. Indeed, we confirmed that the assembled film could maintain very well even after 3000 charge-discharge cycles (Fig. S5).

The electrochemical performance of the *T*-Nb_2O_5/graphene nanocomposite was firstly examined by CV in a three-electrode setup. The CV curves of the *T*-Nb_2O_5/graphene nanocomposite show symmetric anodic and cathodic peaks with very small voltage separation at all scan rates up to 200 mV s^{-1} (Fig. 3a). The broad cathodic and anodic peaks in the potential ranges of 1.0-2.2V from the CV data can be attributed to the following reaction:

$$Nb_2O_5 + xLi+ + xe^- \leftrightarrow Li_xNb_2O_5 \qquad (5)$$

where *x* is the degree of lithium insertion ($0 \le x \le 2$).[11-14] After subtracting the contribution of double-layer capacitance (Fig. S6), the *x* can be determined to be 1.7 at 1 mV s^{-1}, suggesting a high electrochemical ultization of the *T*-Nb_2O_5 nanocrystals.

The kinetic information obtained from CV shoude obey the power law with the relationship $i = av^b$.[48] The calculated *b*-value can be used to distinguish the charge storage whether arises from capacitive or diffusion-controlled processes. While *b*=0.5 represents a semi-infinite diffusion-controlled process (battery type), *b*=1 symbolizes capacitive behavior via a fast faradaic reaction (capacitor type).[6,48,49] By plotting of log(*i*) versus log(*v*) (Fig. 3d), the *b*-values in *T*-Nb_2O_5/graphene nanocomposites close to 1 for both anodic and cathodic peak currents, respectively in a very wide range of sweep rate (from 1 to 200 mV s^{-1}), suggesting a fast Li^+ intercalation process with a capacitive behavior that took place in the Nb_2O_5/graphene nanocomposites. In contrast, the pure *T*-Nb_2O_5 has a *b*-value of 0.8 only in the range of 1 to 10 mV s^{-1} and deviates severely when scan rate is beyond 10 mV s^{-1}, due to poor electronic conductivity of the active materials resulting in the sluggish electron transportation. Thus, it is concluded that the introduction of graphene network improves the electrochemical ulitizaiton and capacitive behavior of T-Nb_2O_5. The total stored energy in the T-Nb_2O_5/graphene nanocomposites arises from an electrochemical process that is not limited by solid state diffusion, similar to what was observed with thin films of Nb_2O_5 microelectrode.[6]

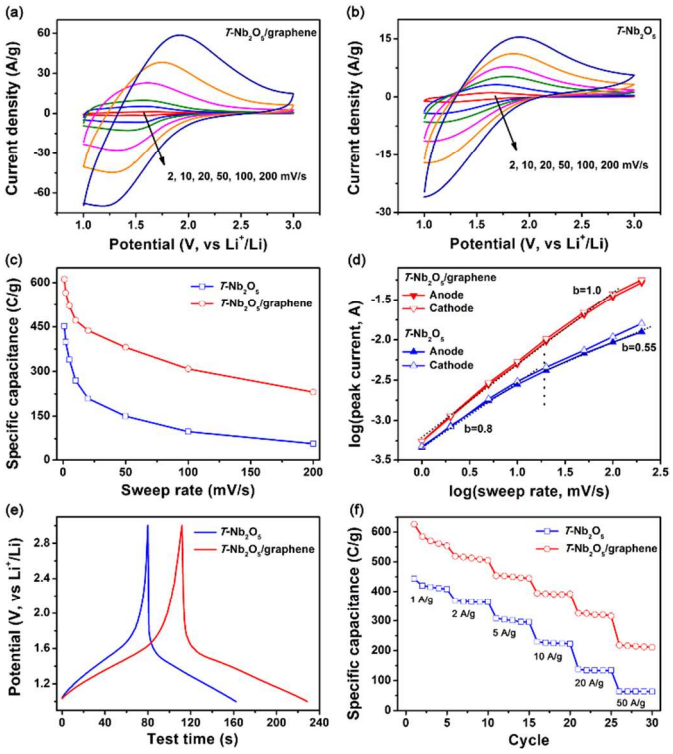

Fig. 3 Cycle voltammetry curves: (a) *T*-Nb_2O_5/graphene electrode and (b) *T*-Nb_2O_5 electrode, (c) charge storage as a function of sweep rate, (d) b-value determination of the peak currents, (e) galvanostatic charge-discharge curves at a current density of 5 A g^{-1}, (f) rate capability from 1 to 50 A g^{-1}. The electrochemical test was operated at potential range 3.0 to 1.0 V in 1 M $LiPF_6$ at room temperature.

Since *T*-Nb_2O_5/graphene nanocomposite is already conductive and may maintain good performances even without the addition of the conductive agents. We therefore prepared a working electrode sulrry by direct mixing of the *T*-Nb_2O_5/graphene nanocomposites with PVDF (90:10) and casted on Cu foils. The conductive-agent-free electrode shows a similar high-rate capaitive behavior at scan rates from 1 to 200 mV s^{-1} (Fig. S7), with the *b*-value of 1 for both anodic and cathodic peak currents. Obviously, higher percent of active

material in the electrode would lead to higher capactiance and energy density in the compacted system. These results further confirm that the conductive *T*-Nb_2O_5/graphene nanocomposites could construct a effective electronic conducting network ensuring that the entire film is electrochemically active. However, compared to the electrode with the conductive agent, the high rate performance decreases slightly. In addition, the electrochemical performance of the *T*-Nb_2O_5/graphene nanocomposites with different graphene contents were also compared (Fig S.8). The *T*-Nb_2O_5/graphene with 25% graphene demonstrated a very similar capacitive and high-rate behavior with the *T*-Nb_2O_5/graphene with 10 % graphene. However, high percent of graphene in the electrode would lead to a little decrease of the total capacitance, due to the decrease of the active materials.

The electrochemical behavior of the *T*-Nb_2O_5/graphene nanocomposite was futher investigated using galvanostatic charge-discharge testing. A comparison for the *T*-Nb_2O_5/graphene nanocomposites and pure *T*-Nb_2O_5 electrodes at a current density of 5 A g^{-1} is displayed in Fig. 3e. The charge-discharge curves exhibits a symmetric slope curve, indicating a reversible lithium intercalation-type electrochemical reaction. The discharge capacitiy of the *T*-Nb_2O_5/graphene nanocomposite electrode is significantly larger than that of pure *T*-Nb_2O_5 electrode, as indicated by the longer discharge time in the former. This result suggests the introduction of conductive graphene has improved the ulitization of electrochemical active sites. The rate performance of *T*-Nb_2O_5/graphene nanocomposite and pure *T*-Nb_2O_5 are further compared in Fig. 3f. The discharge capacities and capacity retentions of the *T*-Nb_2O_5/graphene nanocomposites are much higher than those of the *T*-Nb_2O_5 electrode at all current densities, with the accumulated charge in the former reaches as high as 626 C g^{-1} at 1 A g^{-1} and still retains 220 C g^{-1} at 50 A g^{-1}, comparing to 63 C g^{-1} in *T*-Nb_2O_5, demonstrating the positive effect of graphene on the electrochemical performances. Such a high rate performance is rarely reported for other pseudocapacitive metal oxides. Besides, graphene has also improved the composite' conductivity, as shown in Fig. S9. The Nyquist plot ranging from 100 kHz to 10 mHz features a low faradic charge transfer resistance, indicating the facile Li^+ intercalation redox reaction occured on the *T*-Nb_2O_5/graphene nanocomposite. The low charge transfer resistance can be attributed to the electron transportation highways built up from plane-to-plane graphene network, and the porosity among assembled electrode that is favorable for fast Li ion diffusion.

To maximize the device's power performance, a positive electrode material with similarly high rate response should be developed. Here, we choose two kinds of porous carbons, high-surface area microporous activated carbons (AC) and mesoporous carbons (MC) as electrodes to couple with the *T*-Nb_2O_5/graphene electrode. Their detailed porosity properties are listed in Fig. 4a and Table S2. Typically, the AC are typically microporous materials with the BET speicific surface area of 1973 m^2 g^{-1} and a average pore size of 1.7 nm, and the MC have a BET speicific surface area of 1266 m^2 g^{-1} and a average mesopore size of 6.5 nm. Before constructing into the hybird cells, the carbon electrodes were tested in two-electrode symmetric cells at different current densities (Fig. S10 and Fig. 4b). Their charging/discharging curves are relatively linear and symmetrical, indicating typical characteristic of an ideal supercapacitor. The AC delivers higher specific capactiance at a low current density, while MC performs superior rate performance, making them more suitable to pair with high-rate *T*-Nb_2O_5/graphene electrode.

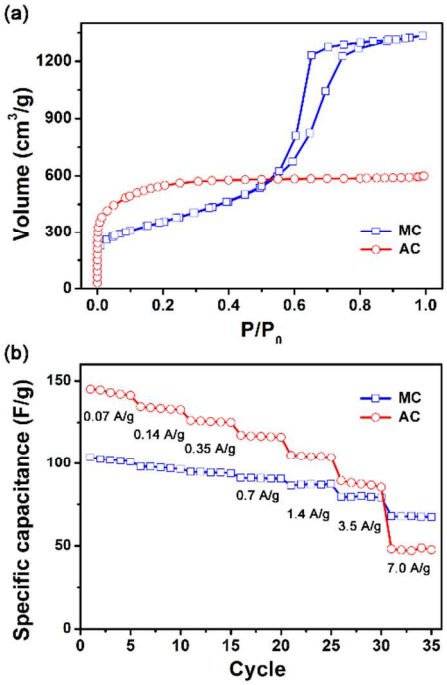

Fig. 4 (a) N_2 adsorption-desorption isotherms of the MC and AC, (b) the rate capability of MC//MC and AC//AC operated at voltage of 0.05 to 3.0 V in 1 M $LiPF_6$ at room temperature.

Two hybrid cells, AC//*T*-Nb_2O_5/graphene and MC//*T*-Nb_2O_5/graphene, were built by using as-prepared *T*-Nb_2O_5/graphene nanocomposites as the negative electrode and AC or MC as the positive electrode. The mass ratios of the two electrodes were optimized to make the charge balance across two electrodes. Here the mass ratio was set to 3.5 for activated carbons couped cells and 3.7 for mesoporous carbons couped cells, making the evenly distributed potential for the two electrode. Note that the specific capacitance and current density values of the supercapacitors reported below are all based on the total mass of the active materials in two electrodes.

Fig. 5 a, b shows the CV curves of the hybrid cells cycled between 0.8 V and 3 V. Both hybrid cells exhibit a relatively quasi-rectangular shape at various scan rates, suggesting the fast electrolyte ions transport and redox pesudocapative behavior. The galvanostatic charge/discharge curves of the hybrid cells and individual potentials of each electrode are recorded in Fig. 5c and 5d respectively. Li^+ ions intercalated into the crystal lattice of *T*-Nb_2O_5 during discharging and extracted into the electrolyte during charging. Correspondingly,

PF_6^- anions adsorbed and desorbed on the carbon electrode, respectively. The charge/discharge curves of the cell display the symmetric quasi-triangular shape, demonstrating the excellent synergistic effect of two different charge storage mechanisms. At 0.2 A g^{-1}, the cell capacitance calculated from the discharge curves reaches 70 F g^{-1} and 80 F g^{-1} for MC//*T*-Nb_2O_5/graphene and AC//*T*-Nb_2O_5/graphene, respectively, and gradually decrease to 32 and 28 F g^{-1}, respectively at 20 A g^{-1}, as shown in Fig. 5e. Obviously, the AC//*T*-Nb_2O_5/graphene cell delivers a high specific capacitance at a low current density, and the MC//*T*-Nb_2O_5/graphene cell performs a better power performance at a high current loading. Both asymmetrical supercapacitors exhibited good cycling stability (>92% of the initial capacitance, Fig. 5f) after ~3000 cycles at 1 A g^{-1}. The Coulombic efficiency approaches ~100% during 3000 cycling (Fig. S11), indicating outstanding electrochmical stability.

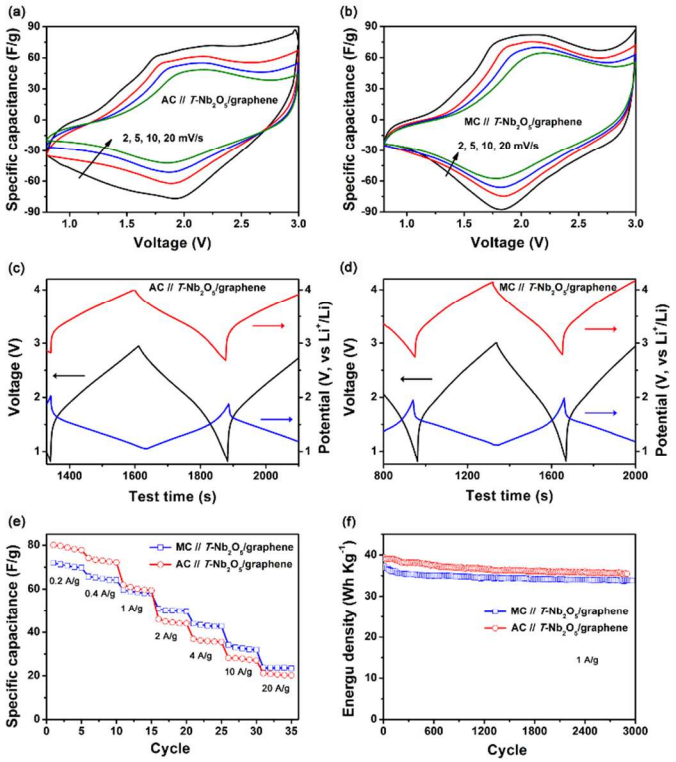

Fig. 5 Cycle voltammetry curves: (a) MC//*T*-Nb_2O_5/graphene and (b) AC//*T*-Nb_2O_5/graphene asymmetric supercapacitors, Galvanostatic charge-discharge curves: (c) MC//*T*-Nb_2O_5/graphene and (d) AC//*T*-Nb_2O_5/graphene asymmetric supercapacitors at a cell current density of 0.2 A g^{-1}, (e) rate capability and (f) cycling performance of MC//*T*-Nb_2O_5/graphene and AC//*T*-Nb_2O_5/graphene asymmetric pseudocapacitor. The asymmetric supercapacitors were tested in 1 M $LiPF_6$ at room temperature.

Fig. 6a shows the Ragone plot (power density vs energy density) of the hybrid supercapacitors as well as the symmetric supercapacitors based on AC and MC for comparison. For AC couped hybrid supercapactior, it exhibited a maximum energy density of 56 Wh kg^{-1} at a power density of 0.58 kW kg^{-1}, and a maximum power density of 16 kW kg^{-1} at an energy density of 13 Wh kg^{-1}. By way of contrast, the MC//*T*-Nb_2O_5/graphene supercapactior gains a slightly lower maximum energy density of 48 kW kg^{-1} at a power density of 0.69 kW kg^{-1}. However, it could deliver a maximum power density of 45 kW kg^{-1} at an energy density of 16 Wh kg^{-1} (discharge time of 1.2 s), which is much better power performance compared with other similar non-aqueous assymmetric supercapactior systems. For example, the AC//CNT-Nb_2O_5 system exhibited an energy density of ~4 Wh kg^{-1} at the maximum power density of 4 kW kg^{-1}.[26] The AC//Nb_2O_5 systhem deliever 40 Wh kg^{-1} and 27 Wh kg^{-1} of total active material at 300 W kg^{-1} (9 minutes) and 1500 W kg^{-1} (1 minute) charge/discharge powers, respectively.[9]

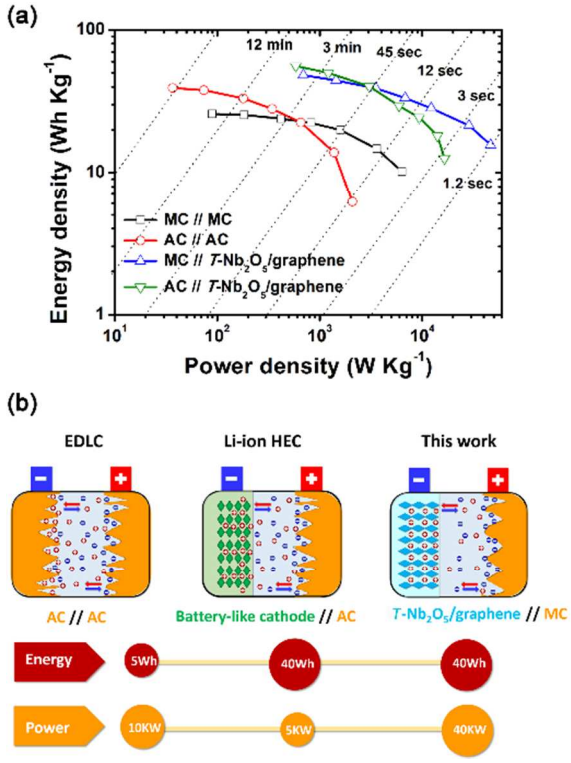

Fig. 6 (a) Ragone plots of asymmetric supercapacitors based on MC//*T*-Nb_2O_5/graphene and AC//*T*-Nb_2O_5/graphene, (b) Schematic diagram of symmetric supercapacitor, Li-ion hybrid electrochemical capacitor and asymmetric supercapacitor based on the MC//*T*-Nb_2O_5/graphene cell.

The impressive energy and power density of our asymmetrical supercapacitors can be attributed to the advanced *T*-Nb_2O_5/graphene electrode materials and the unique pairing. While the *T*-Nb_2O_5 nanocrystals could provide fast two-dimensional Li^+ transport within the bulk crystal structure and exhibit high intercalaction pseudocapacitance, the highly conducting graphene sheets not only accomodate a uniform dispersed *T*-Nb_2O_5 nanocrystals in the network, but allow a rapid and effective charge transport between the *T*-Nb_2O_5 nanocrystals and the current collector, greatly improving the electrochemical utlization of the redox active sites. The layer-by-layer assembled structure of the electrode film are able to hold firmly to the current collector and shorten the diffusion paths for both electrons and ions, resulting in the increase of cycling stability and rate capability. Thus, the synergetic effect between conducting graphene sheets and *T*-Nb_2O_5 nanocrystals

is responsible for the excellent electrochemical performance of the *T*-Nb_2O_5 electrode.

On top of the bilateral benefits from the graphene and *T*-Nb_2O_5, the unique pairing of the mesoporous carbon electrode is also responsible for achieving high energy and power density for the cell. As illustrated in Fig. 6b, the conventional symmetric supercapacitors contain two carbon electrodes aiming to deliver substantial power density, while the lithium-ion asymmetric supercapacitors comprise Li-ion intercalating type electrode and EDLC-forming counter electrode to boost the energy density. Due to the compromise of two different charge storage mechanisms (battery vs EDLC), the asymmetric supercapacitors generaly deliver higher energy density than EDLCs, but at a cost of power density (generally <10 kW kg^{-1}). Herein, we constructed the asymmetric supercapacitors with Li^+ intercalating type *T*-Nb_2O_5/graphene pseduocapative electrodes, which could provide capacities typical of battery materials but at rates even better than those of supercapacitors. Therefore, it is vital to develop high-power counter electrode materials to narrow the kinetics gap between two electrodes to fulfill the demand of high-rate performance for the supercapacitor. The rate performance comparison between MC and AC (Fig. 4b) suggests MC has better power performance, which could be fairly attributed to fast ion transportation and the effective formation of double layer in its mesoporous pore channels. As a result, MC//*T*-Nb_2O_5/graphene asymmetric supercapactior displays higher power handling than the typical AC//AC symmetric supercapacitors or AC//*T*-Nb_2O_5/graphene asymmetric supercapacitors. As we know, the most important characteristic for high performance supercapacitors is to obtain a high energy density and meanwhile remaining an outstanding power density. Thus, our works suggest that the real enhancement for asymmertric supercapacitors lies not only in the development of Li-insertion capactive electrodes but also in high-rate carbon counter electrodes.

4. Conclusions

In summary, we prepare *T*-Nb_2O_5/graphene nanocomposite through a hydrothermal and heat-treatment process method and used as a high-performance pseudocapactive material. The *T*-Nb_2O_5 nanocrystals-anchored graphene can form a layer-by-layer integrated electrode with a developed electron conductive network and shortened ion transport paths, resulting in increased intercalation pseudocapacitance and excellent high-rate capability. With the unique pairing of *T*-Nb_2O_5/graphene pseudocapactive material with mesoporous carbon electrodes, the asymmetrical supercapacitors show high energy and power densities and excellent cycling performance, which could be attributed to the high-rate capacitive behaviors of both Li-intercalation positive electrode and fast ion transportation negative electrodes. The power performance of our supercapacitor reported here can be reached ~45 kW kg^{-1} with a considerable energy density of ~16 Wh kg^{-1}, which exceeds some of the best supercapacitors reported operating in non-aqueous electrolytes. It is expected that this work will not only offer a promising way to develop high-rate supercapacitor electrode materials, but also holds the potential to be applied in the design and construction of the asymmetrical supercapacitors.

Acknowledgements

This work was partly supported by MOST (2014CB239702) and National Science Foundation of China (No. 51302083, No. 51172071, No.51272077), and Fundamental Research Funds for the Central Universities and Shanghai Pujiang Program.

Notes and references

a State Key Laboratory of Chemical Engineering, East China University of Science and Technology, Shanghai 200237, China.
b National Engineering Laboratory for Carbon Fiber Technology, Institute of Coal Chemistry, Chinese Academy of Sciences, Taiyuan 030001, China.
*Corresponding author: Donghui Long, Tel: +86 21 64252924, Fax: +86 21 64252914. E-mail: longdh@mail.ecust.edu.cn; Chunxiang Lv, E-mail: lucx@sxicc.ac.cn.

Electronic Supplementary Information (ESI) available: [Figures S are included in the supplimentary information].
DOI: 10.1039/b000000x/

1 B. E. Conway, *Electrochemical supercapacitors: Scientific fundamentals and technological applications*, Kluwer Academic, 1999.
2 L. L. Zhang and X. S. Zhao, *Chem. Soc. Rev.*, 2009, **38**, 2520.
3 P. Simon and Y. Gogotsi, *Nat. Mater.*, 2008, **7**, 845.
4 V. Augustyn, P. Simon and B, Dunn, *Energy Environ. Sci.*, 2014, **7**, 1597.
5 J. W. Kim, V. Augustyn and B. Dunn, *Adv. Energy. Mater.* 2012, **2**, 141.
6 V. Augustyn, J. Come, M. A. Lowe, J. W. Kim, P. L. Taberna, S. H. Tolbert, H. D. Abruña, P. Simon and B. Dunn, *Nat. Mater.*, 2013, **12**, 518.
7 K. Brezesinski, J. Wang, J. Haetge, C. Reitz, S. O. Steinmueller, S. H. Tolbert, B. M. Smarsly, B. Dunn and T. Brezesinski, *J. Am. Chem. Soc.*, 2010, **132**, 6982-6990.
8 A. Le Viet, M. V. Reddy, R. Jose, B. V. R. Chowdari and S. Ramakrishna, *J. Phys. Chem. C.*, 2010, **114**, 664.
9 J. Come, V. Augustyn, J. W. Kim, P. Rozier, P. L. Taberna, P. Gogotsi, J. W. Long, B. Dunn and P. Simon, *J. Electrochem. Soc.*, 2014, **161**, A718.
10 A. A. Lubimtsev, P. R. C. Kent, B. G. Sumpter and P. Ganesh, *J. Mater. Chem. A*, 2013, **1**, 14951.
11 N. Kumagai, Y. Koishikawa, S. Komaba and N. Koshiba, *J. Electrochem. Soc.*, 1999, **146**, 3203.
12 M. M. Rahman, R. A. Rani, A. Z. Sadek, A. S, Zoolfakar, M. R. Field, T. Ramireddy, K. Kalantar-zadeh and Y. Chen, *J. Mater. Chem. A*, 2013, **1**, 11019.
13 M. Wei, K. Wei, M. Ichihara and H. Zhou, *Electrochem. Commun.*, 2008, **10**, 980.
14 R. Kodama, Y. Terada, I. Nakai, S. Komaba and N. Kumagai, *J. Electrochem. Soc.*, 2006, **153**, A583.
15 R. J. Cava, B. Batlogg, J. J. Krajewski, H. F. Poulsen, P. Gammel, W. F. Peck and L. W. Rupp, *Physical Review B*, 1991, **44**, 6973.

16 D. A. B. de Filho, D. W. Franco, P. P. A. Filho and O. L. Alves, *J. Mater. Sci.*, 1998, **33**, 2607.
17 M. A. Aegerter, *Sol. Energy Mater. Sol. Cells*, 2001, **68**, 401.
18 A. Leela Mohana Reddy and S. Ramaprabhu, *J. Phys. Chem. C*, 2007, **111**, 7727.
19 R.-R. Bi, X.-L. Wu, F.-F. Cao, L.-Y. Jiang, Y.-G. Guo and L.-J. Wan, *J. Phys. Chem. C*, 2010, **114**, 2448.
20 Y. He, W. Chen, X. Li, Z. Zhang, J. Fu, C. Zhao, and E. Xie, *ACS Nano*, 2013, **7**, 174.
21 G. Yu, L. Hu, M. Vosgueritchian, H. Wang, X. Xie, J. R. McDonough, X. Cui, Y. Cui, and Z. Bao, *Nano Letters*, 2011, **11**, 2905.
22 X.-C. Dong, H. Xu, X.-W. Wang, Y.-X. Huang, M. B. Chan-Park, H. Zhang, L.-H. Wang, W. Huang, and P. Chen, *ACS Nano*, 2012, **6**, 3206.
23 Z. Chen, V. Augustyn, J. Wen, Y. Zhang, M. Shen, B. Dunn and Y. Lu, *Adv. Mater.*, 2011, **23**, 791,
24 K.-W. Nam, K.-H. Kim, E.-S. Lee, W.-S. Yoon, X.-Q. Yang, K.-B. Kim, *J. Power Sources*, 2008, **182**, 642.
25 G. Wang, L. Zhang and J. Zhang, *Chem. Soc. Rev.*, 2012, **41**, 797.
26 X. Wang , G. Li , Z. Chen , V. Augustyn , X. Ma , G. Wang, B. Dunn and Y. Lu, *Adv. Energy Mater.*, 2011, **1**, 1089.
27 A. K. Geim, K. S. Novoselov, *Nat. Mater.*, 2007, **6**, 183.
28 A. K. Geim, *Science*, 2009, **324**, 1530.
29 D. R. Dreyer, R. S. Ruoff and C.W. Bielawski, *Angew. Chem. Int. Ed.*, 2010, **49**, 9336.
30 J. Xia , F. Chen , J. Li and N. Tao , *Nat. Nanotechnol.* 2009 , **4** , 505.
31 X. Li, X. Zhang, Z. Li, X. Li, P. Li, P. Sun, X. Lee, R. Zhang, Z. Huang, K. Wang, D. Wu, F. Kang and H. Zhu, *Adv. Funct. Mater.*, 2013, **23**, 4862.
32 X. Zang, Q. Chen, P. Li, Y. He, X. Li, M. Zhu, X. Li, K. Wang, M. Zhong, D. Wu and H. Zhu, *small*, 2014, **10**, 2583.
33 Y. Cao, M. Zhu, P. Li, R. Zhang, X. Li, Q. Gong, K. Wang, M. Zhong, D. Wu, F. Lin and H. Zhu, *Phys. Chem. Chem. Phys.*, 2013,**15**, 19550.
34 Y. W. Zhu, S. Murali, W. W. Cai, X. S. Li, J. W. Suk, J. R. Potts and R. S. Ruoff, *Adv. Mater.*, 2010, **22**, 3906.
35 S. J. Guo, S. J. Dong, *Chem. Soc. Rev.*, 2011, **40**, 2644.
36 Z.-S. Wu, G. M. Zhou, L.-C. Yin, W. C. Ren, F, Li and H.-M. Cheng, *Nano Energy*, 2012, **1**, 107.
37 S. Chen, J. Zhu, X. Wu, Q. Han, and X. Wang, *ACS Nano*, 2010, **4**, 2822-2830.
38 C. Y. Foo, A. Sumboja, D. J. H. Tan, J. X. Wang and P. S. Lee, *Adv. Energy Mater.*, 2014, 1.
39 K. Naoi and P. Simon, *Electrochem. Soc. Interface*, 2008, **17**, 34.
40 C. Liu, F. Li, L.-P. Ma and H.-M. Cheng, *Adv. Mater.*, 2010, **22**, E28.
41 V. Aravindan, W. Chuiling, M. V. Reddy, G. V. Subba Rao, B. V. R. Chowdari and S. Madhavi, *Phys. Chem. Chem. Phys.*, 2012, **14**, 5808.
42 V. Aravindan, W. Chuiling and S. Madhavi, *J. Mater. Chem.*, 2012, **22**, 16026.
43 C. M. Chen, Q. Zhang, C. H. Huang, X. C. Zhao, B. S. Zhang, Q. Q. Kong, M. Z. Wang, Y. G. Yang, R. Cai and D. S. Su, *Chem. Commun.*, 2012, **48**, 7149.
44 H. Chen, F. Sun, J. Wang, W. Li, W. Qiao, L. Ling and D. Long, *J. Phys. Chem. C*, 2013, **117**, 8318.
45 U. Balachandran, N. G. Eror, *J. Mater. Sci. Lett.*, 1982, **1**, 374.
46 M. Palatnikov, O. Shcherbina, N. Sidorov and K. Bormanis, *Ukr. J. Phys. Opt.*, 2012, **13**, 4.
47 S. Stankovich, D. A. Dikin, R. D. Piner, K. A. Kohlhaas, A. Kleinhammes, Y. Jia, Y. Wu, S. T. Nguyen and R. S. Ruoff, *Carbon*, 2007, **45**, 1558.
48 H. Lindstrolm, S. Sodergren, A. Solbrand, H. Rensmo, J. Hjelm, A. Hagfeldt and S.-E. Lindquist, *J. Phys. Chem. B*, 1997, **101**, 7717.
49 J. Wang, J. Polleux, J. Lim and B. Dunn, *J. Phys. Chem. C*, 2007, **111**, 14925.

Graphical abstract

High-Power and High-Energy Asymmetric Supercapacitors Based on Li^+-intercalation into *T*-Nb_2O_5/Graphene Pseduocapative Electrode

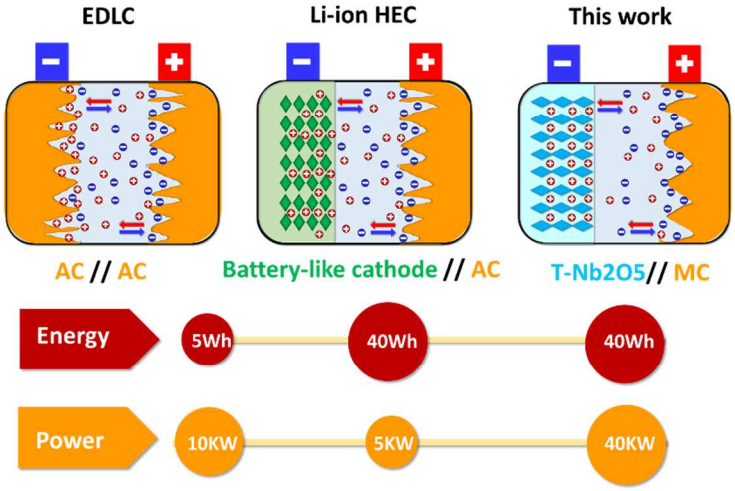

We report a simple hydrothermal and heat-treatment process to fabricate T-Nb2O5/graphene nanocomposite as a high-performance pseudocapactive materials. With the unique pairing of T-Nb2O5/graphene pseudocapactive material with mesoporous carbon electrodes, the asymmetrical supercapacitors show high energy and power densities, and excellent cycling performance.